

# Long Spin Lifetimes in Graphene Spin Valves

Wei Han and R. K. Kawakami<sup>†</sup>

Department of Physics and Astronomy, University of California, Riverside, CA 92521

<sup>†</sup> e-mail: roland.kawakami@ucr.edu

---

Graphene is an attractive material for spintronics due to the possibility of long spin lifetimes arising from low intrinsic spin-orbit coupling<sup>1-5</sup>. However, the longest spin lifetimes measured in single layer graphene (SLG) spin valves are  $\sim 500$  ps for devices with tunneling contacts<sup>6</sup> and less than 200 ps otherwise<sup>7-11</sup>. These spin lifetimes are much shorter than theoretical prediction and have motivated intense theoretical investigations on the possible extrinsic sources of spin scattering in graphene<sup>12-14</sup>. Here, we observe spin lifetimes as long as  $\sim 1$  ns in SLG and  $\sim 6$  ns in bilayer graphene (BLG) with tunneling contacts, which is the highest reported value in a graphene spin valve. By studying the spin lifetime and diffusion coefficient in SLG and BLG as a function of temperature and carrier concentration, we observe sharply contrasting behaviors between the two systems. For SLG, the momentum scattering (e.g. impurity scattering) produces the dominant spin relaxation at low temperatures ( $\leq 100$  K). For BLG, more complicated behavior indicates the relevance of multiple sources of spin relaxation. These results indicate that spin lifetime could potentially become very long in graphene for spintronic applications in logic and storage.

Studies of spin transport and spin relaxation are performed on graphene spin valves (Fig. 1a) consisting of two spin-sensitive Co electrodes (E2, E3) and two Au electrodes (E1, E4). A

critical component is the TiO<sub>2</sub>-seeded MgO tunnel barrier, which isolates the Co from the graphene to greatly reduce the contact-induced spin relaxation<sup>6</sup> (see Methods for details of device fabrication and measurement). For the nonlocal measurement of spin transport, spin-polarized carriers are injected into the graphene at electrode E2<sup>15-21</sup>. The spins subsequently diffuse to electrode E3 where they are detected as a voltage  $V_{NL}$  measured across electrodes E3 and E4<sup>7,10,15-20</sup>. The nonlocal resistance ( $R_{NL} = V_{NL}/I$ ) is measured as a function of in-plane magnetic field (Fig. 1b) to detect the spin injection and transport. Figures 1c and 1d show the nonlocal magnetoresistance (MR) curves for two SLG devices (Device A and Device B), in which the sharp changes in  $R_{NL}$  are due to the magnetization switching of the Co electrodes. The nonlocal MR is indicated by the red arrow in Figure 1c, which is the magnitude of the sharp change in  $R_{NL}$ . Devices A and B have nonlocal MRs of 24  $\Omega$  and 5  $\Omega$  corresponding to spin injection efficiencies of 24% and 7%, respectively<sup>6</sup>.

The spin lifetime ( $\tau_s$ ), diffusion coefficient ( $D$ ), and spin diffusion length ( $\lambda_G = \sqrt{D\tau_s}$ ) are determined by the nonlocal Hanle spin precession measurement (Figure 1e)<sup>16</sup>. Applying an out-of-plane magnetic field ( $H_{\perp}$ ) causes the spins to precess as they diffuse from E2 to E3, which results in characteristic Hanle curves as shown in Figures 1f and 1g for devices A and B at 300 K. The red circles (black circles) are for the parallel (antiparallel) alignment of the Co magnetizations.  $\tau_s$  and  $D$  are determined by fitting the Hanle curves with

$$R_{NL} \propto \pm \int_0^{\infty} \frac{1}{\sqrt{4\pi Dt}} \exp\left[-\frac{L^2}{4Dt}\right] \cos(\omega_L t) \exp(-t/\tau_s) dt \quad (1)$$

where the + (-) sign is for the parallel (antiparallel) magnetization state,  $L$  is the spacing between the Co electrodes,  $\omega_L = g\mu_B H_{\perp}/\hbar$  is the Larmor frequency,  $g$  is the g-factor,  $\mu_B$  is the Bohr magneton, and  $\hbar$  is the reduced Planck's constant. For device A, the best fit parameters are  $D =$

0.020 m<sup>2</sup>/s and  $\tau_s = 771$  ps, which yields  $\lambda_G = 3.9$   $\mu\text{m}$ . For device B,  $D = 0.013$  m<sup>2</sup>/s,  $\tau_s = 447$  ps, and  $\lambda_G = 2.4$   $\mu\text{m}$ .

Figures 2a and 2b show the 300 K nonlocal MR loops and Hanle spin precession curves for device B at different carrier concentrations. The carrier concentration is tuned by gate voltage ( $V_g$ ) and is given by  $n = -\alpha(V_g - V_{\text{CNP}})$  where  $\alpha = 7.2 \times 10^{10}$  cm<sup>-2</sup> V<sup>-1</sup> for a 300 nm SiO<sub>2</sub> dielectric layer and  $V_{\text{CNP}}$  is the gate voltage for charge neutrality<sup>11,22</sup>. Figure 2c summarizes the nonlocal MR (black squares) and SLG conductivity (red line) as a function of gate voltage. The peak in nonlocal MR at the charge neutrality point is consistent with previous studies on tunneling spin injection<sup>6,23-25</sup>. The  $\tau_s$  and  $D$  obtained from the Hanle curves are plotted as a function of gate voltage in Figure 2d. At 300 K, there is no obvious correlation between  $\tau_s$  and  $D$ . Interestingly, when the device is cooled to  $T = 4$  K,  $\tau_s$  and  $D$  exhibit a strong correlation, with both quantities increasing with carrier concentration (Fig. 2f). One consequence of this increase is the enhancement of the nonlocal MR at high carrier concentrations (Fig. 2e). More importantly, the correlation of  $\tau_s$  and  $D$  implies a linear relation between  $\tau_s$  and the momentum scattering time,  $\tau_p$  ( $D \sim \tau_p$  as discussed in ref. 8). This indicates that at low temperatures the spin scattering is dominated by momentum scattering through the Elliot-Yafet (EY) mechanism (i.e. finite probability of a spin-flip during a momentum scattering event)<sup>26-28</sup>.

The temperature dependences of  $\tau_s$  and  $D$  at different carrier concentrations are shown in Figures 3a and 3b. As the temperature decreases from 300 K to 4 K,  $\tau_s$  shows a modest increase at higher carrier densities (e.g. from  $\sim 0.5$  ns to  $\sim 1$  ns for  $V_g - V_{\text{CNP}} = +60$  V) and little variation for lower carrier densities. The temperature dependence of  $D$  shows a similar behavior as  $\tau_s$ . To analyze the relationship between the spin scattering and momentum scattering, we plot  $\tau_s$  vs.  $D$  for temperatures below or equal to 100 K (Fig. 3c) and for temperatures above 100 K (Fig. 3d).

The main trend is that for lower temperatures (Fig. 3c),  $\tau_s$  scales linearly with  $D$ , which indicates that an EY spin relaxation mechanism is dominant at lower temperatures ( $\leq 100$  K). For higher temperatures (Fig. 3d),  $\tau_s$  and  $D$  do not follow the linear relationship as shown at low temperatures, which suggests that multiple sources of spin scattering are present. If there is more than one source of EY spin scattering (e.g. impurities of different species, phonons, etc.), the linear relationship between  $\tau_s$  and  $\tau_p$  does not necessarily hold; for example, with two EY scattering mechanisms obeying  $\tau_{s,1}^{-1} = k_1 \tau_{p,1}^{-1}$  and  $\tau_{s,2}^{-1} = k_2 \tau_{p,2}^{-1}$ , the overall spin relaxation rate

$\tau_s^{-1} = \tau_{s,1}^{-1} + \tau_{s,2}^{-1} = k_1 \left( \tau_{p,1}^{-1} + \frac{k_2}{k_1} \tau_{p,2}^{-1} \right)$  is not proportional to the overall momentum scattering rate  $\tau_p^{-1} = \tau_{p,1}^{-1} + \tau_{p,2}^{-1}$  except in some special cases (e.g.  $k_1 = k_2$ ,  $\tau_{p,1} \ll \tau_{p,2}$ , etc.).

Next, we investigate the spin relaxation in BLG spin valves. BLG is identified by atomic force microscopy and micro-Raman spectroscopy<sup>29</sup>. Figure 4a shows a representative nonlocal MR curve of a BLG spin valve (Device C,  $L=3.05$   $\mu\text{m}$ ) measured at 300 K (the nonlocal MR is 0.6  $\Omega$  at  $V_g = V_{\text{CNP}}$ ). Figure 4b shows the corresponding Hanle curve at 300 K with best fit parameters of  $D = 0.008$   $\text{m}^2/\text{s}$  and  $\tau_s = 268$  ps. Figure 4d shows the Hanle curve of the longest observed spin lifetime of 6.2 ns, which is obtained on device C for the charge neutrality point at 20 K. Figure 4c and 4e show the Hanle curves at 20 K for gate voltages of  $V_{\text{CNP}} - 40$  V and  $V_{\text{CNP}} + 40$  V, respectively. The gate dependences of  $\tau_s$  and  $D$  at 300 K and 20 K are shown in Figure 4f and 4g, respectively. At 300 K,  $\tau_s$  varies from 250 ps to 450 ps as a function of gate voltage and exhibits no obvious correlation with  $D$ . At 20 K,  $\tau_s$  varies from 2.5 ns to 6.2 ns, showing a peak at the charge neutrality point. On the other hand, the gate dependence of  $D$  exhibits lower values near the charge neutrality point and increasing values at higher carrier densities. This opposite trend of  $\tau_s$  and  $D$  is robust even under an irreversible sample change experienced by this

device<sup>30</sup>. The opposite behaviors of  $\tau_s$  and  $D$  suggest the importance of D'yakonov-Perel (DP) spin relaxation (i.e. spin relaxation via precession in internal spin-orbit fields) where  $\tau_s$  scales inversely with  $\tau_p$ <sup>28,31</sup>.

Figures 5a and 5b show the temperature dependences of  $\tau_s$  and  $D$ , respectively. At low temperatures,  $\tau_s$  is enhanced while  $D$  is reduced. This behavior of  $D$  is consistent with the thermally activated carriers in BLG, as demonstrated by the temperature dependence of BLG conductivity (Fig. 5b inset)<sup>32</sup>. The opposite trends of the temperature dependences of  $\tau_s$  and  $D$  suggest the strong contributions of spin relaxation mechanisms of the DP type. However, a detailed analysis of  $\tau_s$  vs.  $D$  (similar to Fig. 3c and 3d for SLG) does not yield a clear scaling between the two quantities. In addition, there are more sample-to-sample variations in BLG (compared to SLG) including devices without enhanced  $\tau_s$  at low temperature. These characteristics are probably due to the relevance of multiple sources of spin relaxation in BLG, unlike SLG where a single dominant EY spin relaxation mechanism generates a linear scaling of  $\tau_s$  and  $D$  at low temperatures.

Comparing SLG and BLG, one interesting behavior is the longer spin lifetimes observed in BLG (up to 6.2 ns) than in SLG (up to 1.0 ns). Theoretically, the intrinsic spin-orbit coupling in BLG is an order of magnitude larger than in SLG, which predicts shorter spin lifetimes for BLG<sup>33</sup>. The opposite experimental trend verifies that the spin relaxation in graphene is of extrinsic origin, with SLG more sensitive to the extrinsic spin scattering than BLG. Another interesting observation is the contrasting relationships between  $\tau_s$  and  $D$  for SLG and BLG. For SLG,  $\tau_s$  scales linearly with  $D$  at low temperatures ( $\leq 100$  K), indicating the dominance of EY spin relaxation in SLG. For BLG,  $\tau_s$  displays an opposite trend to  $D$  which indicates the importance of DP spin relaxation. Theoretically, the DP-type spin relaxation could originate

from curvature in the graphene, which generates internal spin-orbit fields<sup>1,14</sup>. Experimentally, ripples are known to be present in graphene on SiO<sub>2</sub> substrates, so the DP-type spin relaxation should be present in both the SLG and BLG. For SLG, however, the presence of a much stronger EY spin relaxation dominates the DP contribution to generate the observed linear scaling between  $\tau_s$  and  $D$ . For BLG, the EY spin relaxation is weaker and the lack of clear inverse scaling of  $\tau_s$  and  $D$  suggests that both EY and DP contributions are relevant. The weaker contribution of EY to BLG as compared to the SLG makes impurity scattering from surface impurities or defects a primary candidate as the source of the dominant EY spin relaxation for two reasons: (1) BLG is less surface sensitive than SLG due to its larger thickness, (2) BLG is more effective at screening an impurity potential than SLG<sup>34</sup>.

In summary, spin lifetimes as long as  $\sim 1$  ns in SLG and  $\sim 6$  ns in BLG are observed by taking advantage of tunneling contacts to reduce the contact-induced spin relaxation. By studying the spin lifetime and diffusion coefficient in SLG and BLG as a function of temperature and carrier concentration, contrasting behaviors are observed. For SLG, one source of EY spin scattering (e.g. impurity scattering) is dominant at low temperatures leading to the linear scaling of  $\tau_s$  and  $\tau_p$ . For BLG, the complicated behavior between  $\tau_s$  and  $D$  indicates the relevance of both EY and DP spin relaxation mechanisms.

*Note.* Related results have recently been posted<sup>35,36</sup>.

## Methods

### Device fabrication and measurement

The graphene flakes are mechanically exfoliated from HOPG onto an SiO<sub>2</sub> (300 nm thickness)/Si substrate<sup>37</sup>. SLG and BLG are identified by optical microscopy and Raman spectroscopy. Standard e-beam lithography with PMMA/MMA bilayer resist is used to define the Au and Co electrodes. First, two Au electrodes are put down on the two ends of the graphene. Then a second step of e-beam lithography is used for the Co electrodes, where subsequent angle evaporations of TiO<sub>2</sub>, MgO, and Co produce the ferromagnetic electrodes with tunneling contacts<sup>6</sup>. In ultrahigh vacuum, 0.12 nm of Ti is deposited at an angle of 9° and is converted to TiO<sub>2</sub> by exposure to oxygen partial pressure of 5×10<sup>-8</sup> torr for 30 min. A 0.8 nm layer of MgO is deposited at 9° for the tunnel barrier and 3 nm of MgO is deposited at 0° for a masking layer. 80 nm of Co is deposited at 7° for the ferromagnetic electrodes, which are capped with 5 nm of Al<sub>2</sub>O<sub>3</sub> prior to lift-off. The Ti, MgO, and Al<sub>2</sub>O<sub>3</sub> are deposited by electron beam evaporation and the Co is deposited from a thermal effusion cell. Typically several Co electrodes are fabricated in between the two Au electrodes, but only two Co electrodes are wired up for the nonlocal measurement. The widths of the Co electrodes vary between 80 nm and 300 nm to have different coercivities.

Samples are measured in a variable temperature He<sup>4</sup> cryostat with superconducting magnet. Nonlocal voltages ( $V_{NL}$ ) are measured using lock-in detection with an ac injection current of  $I = 1 \mu\text{A}$  rms at 13 Hz. The gate voltage is applied to the degenerately doped Si substrate. A constant background level is subtracted from  $R_{NL}$ .

### Acknowledgements

We acknowledge technical assistance and discussion with K. M. McCreary, H. Wen, J. J. I. Wong, A. G. Swartz, K. Pi and Y. Li and the support of ONR (N00014-09-1-0117), NSF (DMR-1007057), and NSF (MRSEC DMR-0820414).

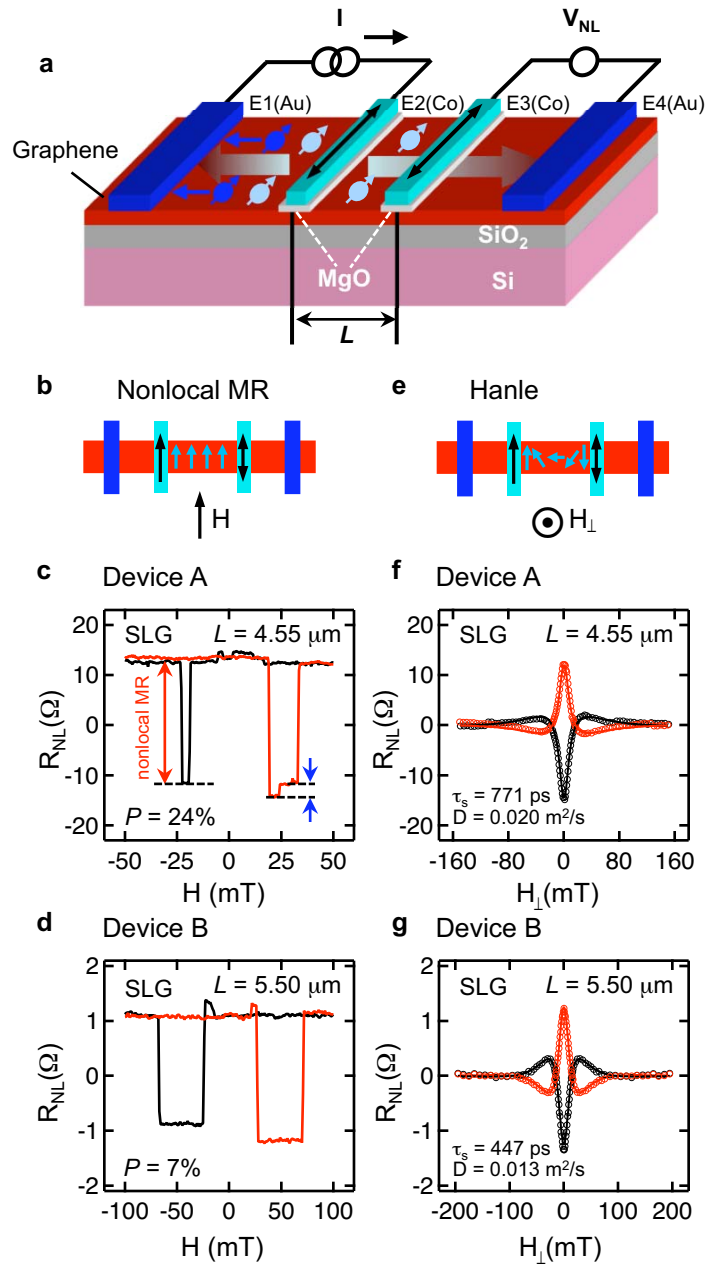
## References:

- 1 Huertas-Hernando, D., Guinea, F., & Brataas, A., Spin-orbit coupling in curved graphene, fullerenes, nanotubes, and nanotube caps. *Phys. Rev. B* 74, 155426 (2006).
- 2 Min, H., Hill, J.E., Sinitsyn, N.A., Sahu, B.R., Kleinman, L., & MacDonald, A.H., Intrinsic and Rashba spin-orbit interactions in graphene sheets. *Phys. Rev. B* 74, 165310 (2006).
- 3 Yao, Y., Ye, F., Qi, X.-L., Zhang, S.-C., & Fang, Z., Spin-orbit gap of graphene: First-principles calculations. *Phys. Rev. B* 75, 041401(R) (2007).
- 4 Trauzettel, B., Bulaev, D.V., Loss, D., & Burkard, G., Spin qubits in graphene quantum dots. *Nature Physics* 3, 192-196 (2007).
- 5 Restrepo, O.D. & Windl, W., Ultimate spin relaxation time in group-IV materials. *arXiv:1010.5436* (2010).
- 6 Han, W., Pi, K., McCreary, K.M., Li, Y., Wong, J.J.I., Swartz, A.G., & Kawakami, R.K., Tunneling Spin Injection into Single Layer Graphene. *Phys. Rev. Lett.* 105, 167202 (2010).
- 7 Tombros, N., Jozsa, C., Popinciuc, M., Jonkman, H.T., & van Wees, B.J., Electronic spin transport and spin precession in single graphene layers at room temperature *Nature* 448, 571-574 (2007).
- 8 Józsa, C., Maassen, T., Popinciuc, M., Zomer, P.J., Veligura, A., Jonkman, H.T., & van Wees, B.J., Linear scaling between momentum and spin scattering in graphene. *Phys. Rev. B* 80, 241403(R) (2009).
- 9 Popinciuc, M., Jozsa, C., Zomer, P.J., Tombros, N., Veligura, A., Jonkman, H.T., & van Wees, B.J., Electronic spin transport in graphene field effect transistors. *Phys. Rev. B* 80, 214427 (2009).
- 10 Han, W., Pi, K., Bao, W., McCreary, K.M., Li, Y., Wang, W.H., Lau, C.N., & Kawakami, R.K., Electrical detection of spin precession in single layer graphene spin valves with transparent contacts. *Appl. Phys. Lett.* 94, 222109 (2009).
- 11 Pi, K., Han, W., McCreary, K.M., Swartz, A.G., Li, Y., & Kawakami, R.K., Manipulation of Spin Transport in Graphene by Surface Chemical Doping. *Phys. Rev. Lett.* 104, 187201 (2010).
- 12 Ertler, C., Konschuh, S., Gmitra, M., & Fabian, J., Electron spin relaxation in graphene: The role of the substrate. *Phys. Rev. B* 80, 041405(R) (2009).
- 13 Castro Neto, A.H. & Guinea, F., Impurity-Induced Spin-Orbit Coupling in Graphene. *Phys. Rev. Lett.* 103, 026804 (2009).
- 14 Huertas-Hernando, D., Guinea, F., & Brataas, A., Spin-Orbit-Mediated Spin Relaxation in Graphene. *Phys. Rev. Lett.* 103, 146801 (2009).

- 15 Johnson, M. & Silsbee, R.H., Interfacial charge-spin coupling: Injection and detection of  
spin magnetization in metals. *Phys. Rev. Lett.* 55, 1790–1793 (1985).
- 16 Jedema, F.J., Heersche, H.B., Filip, A.T., Baselmans, J.J.A., & van Wees, B.J., Electrical  
detection of spin precession in a metallic mesoscopic spin valve. *Nature* 416, 713-716  
(2002).
- 17 Lou, X., Adelman, C., Crooker, S.A., Garlid, E.S., Zhang, J., Reddy, K.S.M., Flexner,  
S.D., Palmstrom, C.J., & Crowell, P.A., Electrical detection of spin transport in lateral  
ferromagnet-semiconductor devices. *Nature Physics* 3, 197-202 (2007).
- 18 Cho, S., Chen, Y.-F., & Fuhrer, M.S., Gate-tunable graphene spin valve. *Appl. Phys. Lett.*  
91, 123105 (2007).
- 19 Shiraishi, M., Ohishi, M., Nouchi, R., Nozaki, T., Shinjo, T., & Suzuki, Y., Robustness  
of Spin Polarization in Graphene-based Spin Valves. *Adv. Funct. Mater.* 19, 3711-3716  
(2009).
- 20 Goto, H., Kanda, A., Sato, T., Tanaka, S., Ootuka, Y., Odaka, S., Miyazaki, H.,  
Tsukagoshi, K., & Aoyagi, Y., Gate control of spin transport in multilayer graphene. *Appl.*  
*Phys. Lett.* 92, 212110 (2008).
- 21 Han, W., Wang, W.H., Pi, K., McCreary, K.M., Bao, W., Li, Y., Miao, F., Lau, C.N., &  
Kawakami, R.K., Electron-Hole Asymmetry of Spin Injection and Transport in Single-  
Layer Graphene. *Phys. Rev. Lett.* 102, 137205 (2009).
- 22 Geim, A.K. & Novoselov, K.S., The rise of graphene. *Nature Materials* 6, 183-191  
(2007).
- 23 Takahashi, S. & Maekawa, S., Spin injection and detection in magnetic nanostructures.  
*Phys. Rev. B* 67, 052409 (2003).
- 24 Fert, A. & Jaffres, H., Conditions for efficient spin injection from a ferromagnetic metal  
into a semiconductor. *Phys. Rev. B* 64, 184420 (2001).
- 25 Jaffres, H., George, J.-M., & Fert, A., Spin transport in multiterminal devices: Large spin  
signals in devices with confined geometry. *Phys. Rev. B* 82, 140408(R) (2010).
- 26 Elliott, R.J., Theory of the Effect of Spin-Orbit Coupling on Magnetic Resonance in  
Some Semiconductors. *Phys. Review* 96, 266 (1954).
- 27 Yafet, Y. in *Solid State Physics*, edited by F. Seitz and D. Turnbull (Academic Press Inc.,  
New York, 1963), Vol. 14, p. 1.
- 28 Meier, F. & Zacharenya, B.P. *Optical Orientation, Modern Problems in Condensed*  
*Matter Science (North-Holland, Amsterdam, 1984), Vol. 8.*
- 29 Ferrari, A.C., Meyer, J.C., Scardaci, V., Casiraghi, C., Lazzeri, M., Mauri, F., Piscanec,  
S., Jiang, D., Novoselov, K.S., Roth, S., & Geim, A.K., Raman Spectrum of Graphene  
and Graphene Layers. *Phys. Rev. Lett.* 97, 187401 (2006).
- 30 *See supplementary material for detailed descriptions.*
- 31 D'yakonov, M.I. & Perel', V.I. *Sov. Phys. State* 13, 3023 (1972).
- 32 Morozov, S.V., K.S. Novoselov, Katsnelson, M.I., Schedin, F., Elias, D.C., Jaszczak, J.A.,  
& Geim, A.K., Giant Intrinsic Carrier Mobilities in Graphene and Its Bilayer. *Phys. Rev.*  
*Lett.* 100, 016602 (2008).
- 33 Guinea, F., Spin-orbit coupling in a graphene bilayer and in graphite. *New J. of Phys.* 12,  
083063 (2010).
- 34 Guinea, F., Charge distribution and screening in layered graphene systems. *Phys. Rev. B*  
75, 235433 (2007).

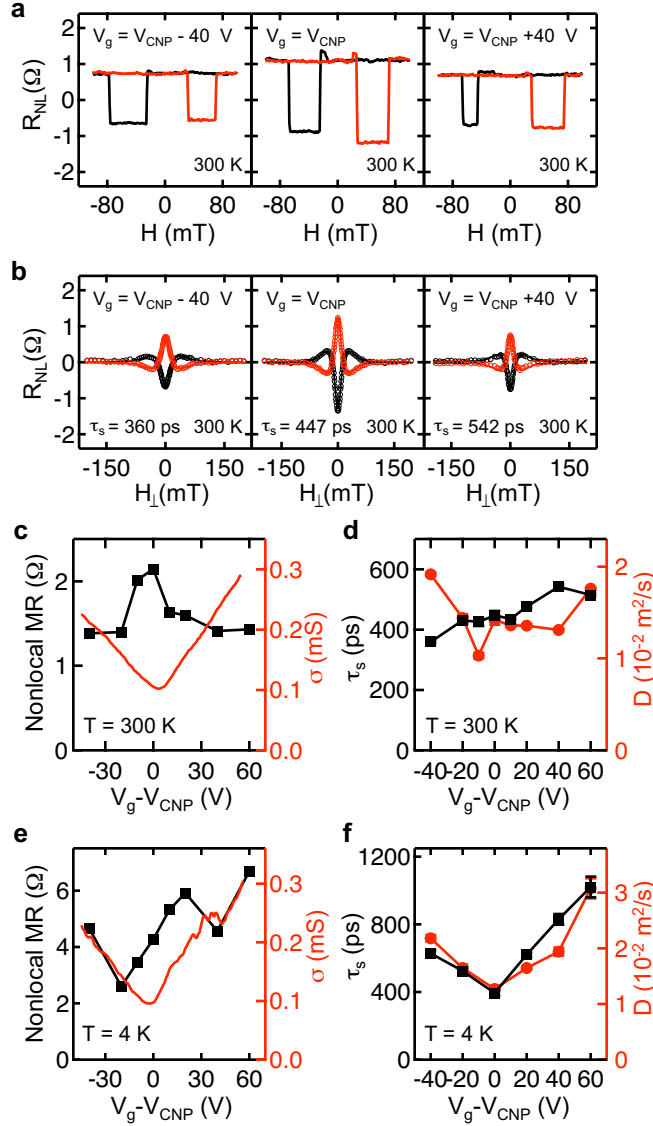
- 35 Yang, T.-Y., Balkrishna, J., Volmer, F., Avsar, A., Jaiswal, M., Samm, J., Ali, S.R.,  
Pachoud, A., Zeng, M., Popinciuc, M., Guntherodt, G., Beschoten, B., & Ozyilmaz, B.,  
Observation of Long Spin Relaxation Times in Bilayer Graphene at Room Temperature.  
*arXiv:1012.1156* (2010).
- 36 Maassen, T., Dejene, F.K., Guimaraes, M.H., Jozsa, C., & van Wees, B.J., Comparison  
between charge and spin transport in few layer graphene. *arXiv:1012.0526* (2010).
- 37 Novoselov, K.S., Geim, A.K., Morozov, S.V., Jiang, D., Zhang, Y., Dubonos, S.V.,  
Grigorieva, I.V., & Firsov, A.A., Electric Field Effect in Atomically Thin Carbon Films.  
*Science* 306, 666-669 (2004).

Figure 1



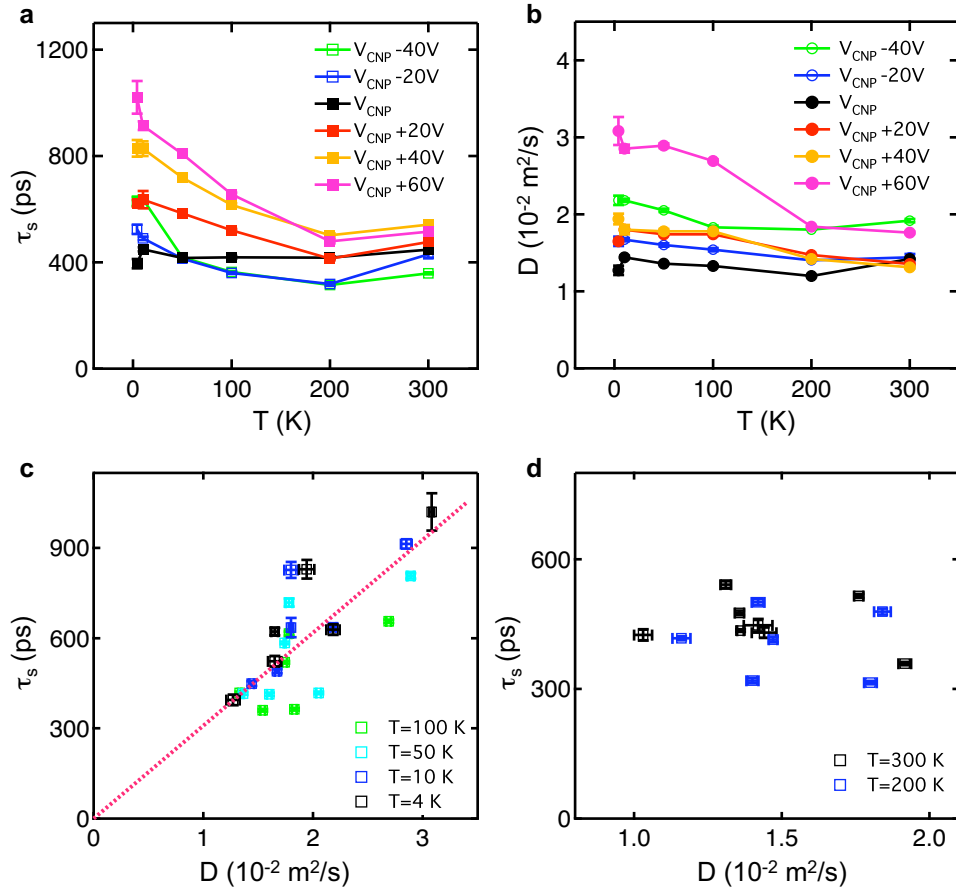
**Fig. 1. Measurement of spin transport and spin relaxation.** (a) Schematic device geometry for a graphene spin valve. Actual devices consist of several Co electrodes between the Au electrodes, but only two Co electrodes wired up for the nonlocal measurement. (b) Nonlocal MR measurements to detect spin injection and transport in graphene. An in-plane magnetic field is applied to achieve parallel and antiparallel alignments of the Co magnetizations. (c, d) Nonlocal MR measurement of device A (SLG) and device B (SLG), respectively, at 300 K. The red (black) curve is measured as the field is swept up (down). The large change in  $R_{NL}$  indicated by the red arrow is due to the switching of the Co magnetization. The additional small jump indicated by the blue arrows is due to the magnetization switching from an unwired Co electrode, which verifies the presence of a weak but non-zero interaction between the graphene carriers and the Co electrode (e.g. interfacial spin scattering, fringe field, etc.). (e) Hanle measurement to determine the spin lifetime and diffusion coefficient. An out-of-plane magnetic field is applied to induce spin precession as the spins diffuse from E2 to E3. (f, g) Hanle measurements of device A and device B, respectively, at 300 K. The red (black) circles are data taken for parallel (antiparallel) Co magnetizations. The solid lines are the best fit by equation 1.

Figure 2



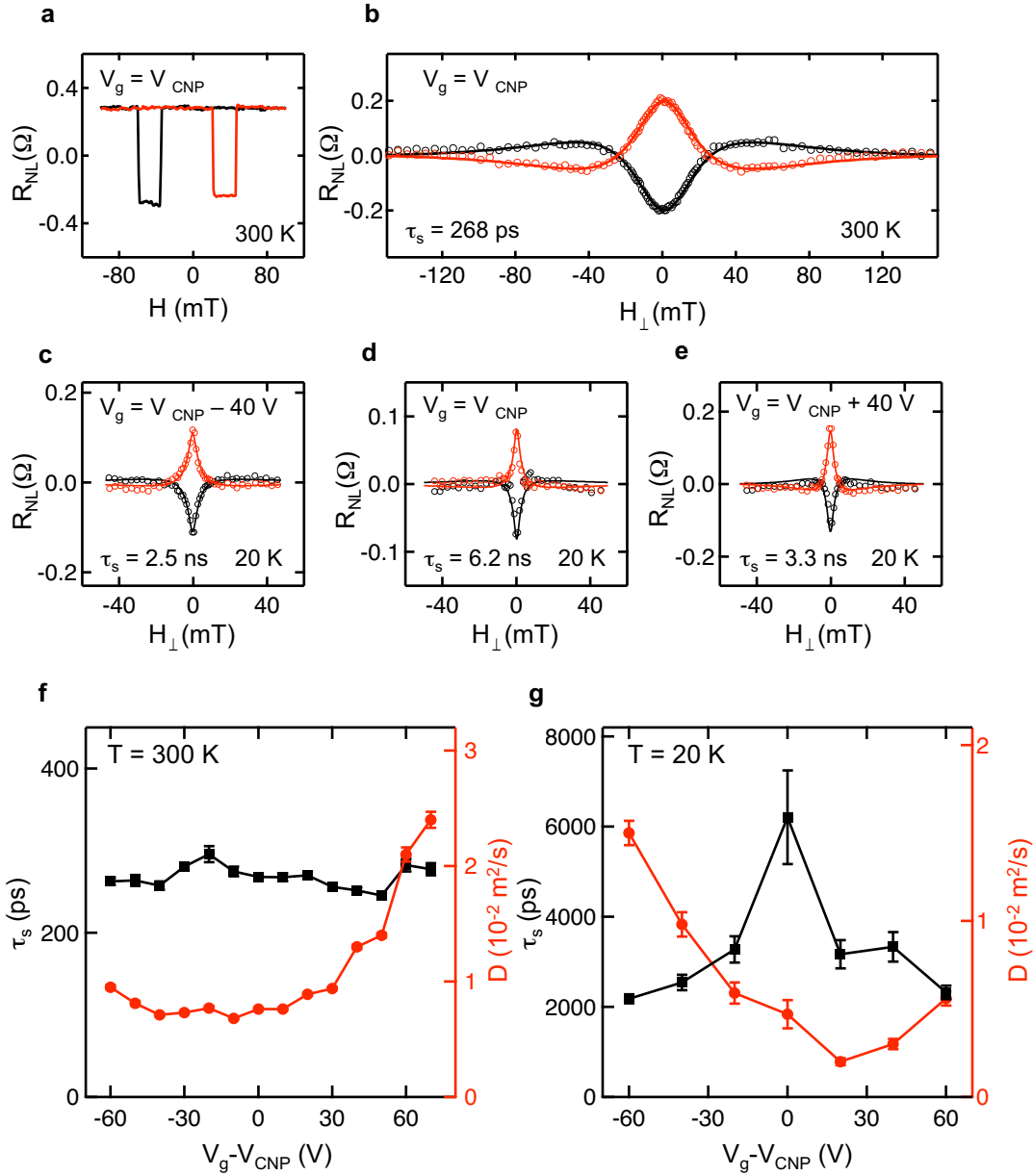
**Fig. 2. Gate dependence of SLG spin valves.** (a) Nonlocal MR measurements of device B at 300 K for different gate voltages. (b) Hanle measurements of device B at 300 K for different gate voltages. (c) Nonlocal MR (black squares) and SLG conductivity (red curve) as a function of gate voltage at 300 K. (d) Spin lifetime (black squares) and diffusion coefficient (red circles) as a function of gate voltage at 300 K. (e) Nonlocal MR (black squares) and SLG conductivity (red curve) as a function of gate voltage at 4 K. (f) Spin lifetime (black squares) and diffusion coefficient (red circles) as a function of gate voltage at 4 K.

Figure 3



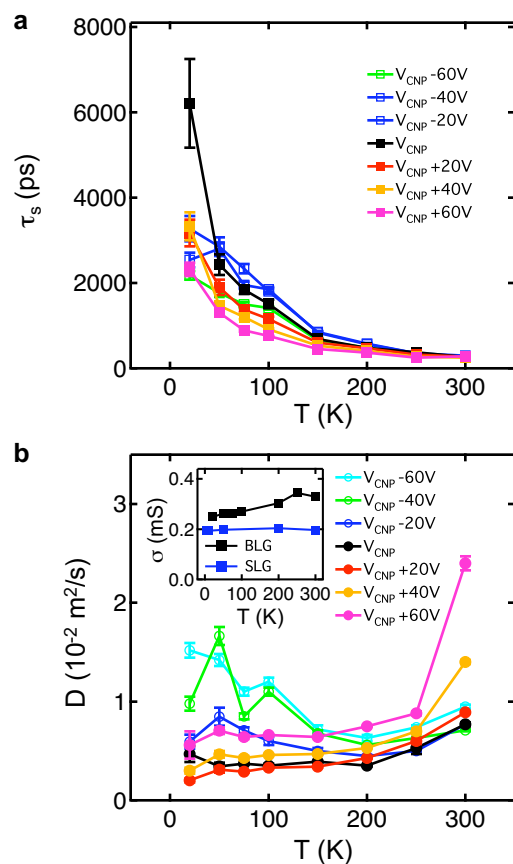
**Fig. 3. Temperature dependence of SLG spin valves.** (a) Temperature dependence of the spin lifetime at different gate voltages for device B. (b) Temperature dependence of the diffusion coefficient at different gate voltages for device B. (c) Plot of spin lifetime vs. diffusion coefficient for  $T \leq 100 \text{ K}$ . The dashed line shows the best linear fit. (d) Plot of spin lifetime vs. diffusion coefficient for  $T \geq 200 \text{ K}$ .

Figure 4



**Fig. 4. Gate dependence of BLG spin valves.** (a) Nonlocal MR measurement of device C (BLG) at 300 K ( $L = 3.05 \mu\text{m}$ ). (b) Hanle measurement for device C at 300 K for  $V_g = V_{\text{CNP}}$ . (c, d, e) Hanle measurement for device C at 20 K for  $V_g - V_{\text{CNP}} = -40$  V, 0 V, and +40 V, respectively. (f) Spin lifetime (black squares) and diffusion coefficient (red circles) as a function of gate voltage at 300 K. (g) Spin lifetime (black squares) and diffusion coefficient (red circles) as a function of gate voltage at 20 K.

Figure 5



**Fig. 5. Temperature dependence of BLG spin valves.** (a) Temperature dependence of spin lifetime at different gate voltages for device C. (b) Temperature dependence of diffusion coefficient at different gate voltages for device C. Inset: temperature dependence of the graphene conductivity at the charge neutrality point for BLG device C (black squares) and SLG device B (blue squares).

# Long Spin Lifetimes in Graphene Spin Valves

Wei Han and R. K. Kawakami<sup>†</sup>

Department of Physics and Astronomy, University of California, Riverside, CA 92521

<sup>†</sup> e-mail: roland.kawakami@ucr.edu

---

## Supplementary Materials

### Robustness of gate-dependent behavior of $\tau_s$ and $D$ in BLG spin valves

Graphene spin valves occasionally experience an abrupt, irreversible change in device characteristics. Such an event occurred while studying the temperature dependence of BLG device C between 10 K and 20 K. Figure S1a shows the Hanle curve at 10 K at the charge neutrality point. The curve fit yields  $\tau_s = 4.4$  ns and  $D = 0.0022$  m<sup>2</sup>/s. Figure S1b shows the gate dependence of  $\tau_s$  and  $D$ . At 10 K,  $\tau_s$  varies from 2.1 ns to 4.4 ns with a peak at the charge neutrality point, while  $D$  exhibits lower values near the charge neutrality point and increasing values at higher carrier densities. Comparing with the 20 K data in Figure 4g, this indicates that both the long spin lifetime and the opposite gate-dependent behaviors of  $\tau_s$  and  $D$  are robust to the irreversible device change.

Figure S1

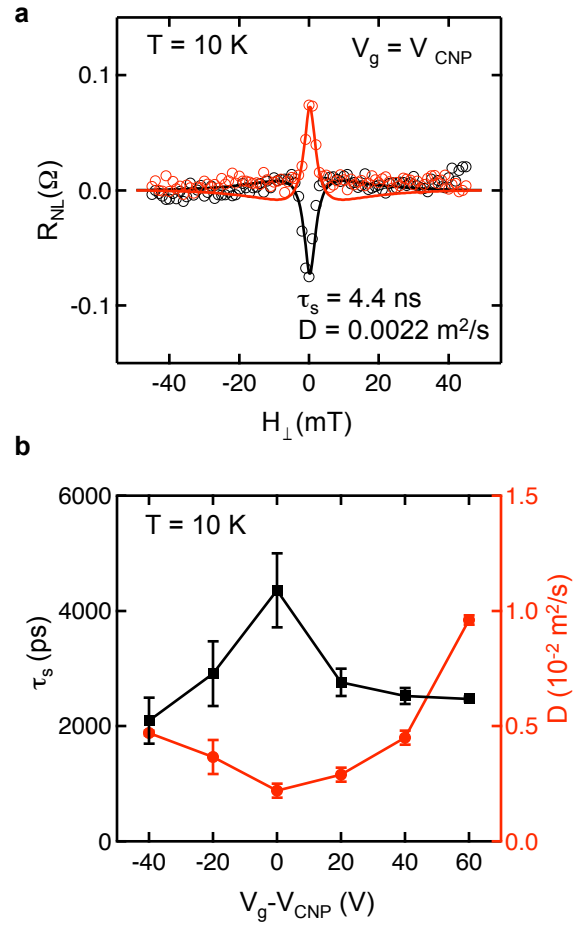


**Fig. S1. 10 K results of the BLG spin valve (device C).** (a) Hanle measurements of device C at 10 K at the charge neutrality point. (b) Spin lifetime (black points) and diffusion coefficient (red points) as a function of gate voltage at 10 K.